MITSUBISHI ELECTRIC RESEARCH LABORATORIES
https://www.merl.com

Simulator-based Mission Optimization for Conceptual Aircraft Design with Turboelectric Propulsion

Hu, Hanyao; Menner, Marcel; Wang, Yebin; Fang, Huazhen; Sun, Dengfeng; Takegami, Tomoki

TR2023-069 June 13, 2023

Abstract

The electrification of pneumatic or hydraulic system on aircraft has been shown effective in reducing the fuel burn. Recently, electrifying propulsive loads has attracted a lot of attention to further improve fuel economy. This work focuses on tools to facilitate more electric aircraft at conceptual design stage, particularly assuming a turbo-generator architecture. Specifically, we develop a simulation tool, mimicking SUAVE [1], which allows mission and fuel burn analysis. Major differences from SUAVE include more detailed models of components in the electric propulsive branch and degrees of freedom to adjust the velocity profile along the entire mission. Based on the simulator, this work further proposes to leverage a gradient-free optimization technique, which optimizes the optimal velocity profile along the entire mission to minimize fuel burn. Simulation results on two aircraft designs, a conventional Boeing 737-800 and NASA-STARC-ABL, verify the effectiveness of the proposed tools.

AIAA/IEEE Electric Aircraft Technologies Symposium (EATS) 2023

Mitsubishi Electric Research Laboratories, Inc.
201 Broadway, Cambridge, Massachusetts 02139

Simulator-based Mission Optimization for Conceptual Aircraft Design with Turboelectric Propulsion

Hanyao Hu*
Purdue University, West Lafayette, IN 47907

Marcel Menner†, Yebin Wang‡
Mitsubishi Electric Research Laboratories, Cambridge, MA, 02139

Huazhen Fang§
University of Kansas, Lawrence, KS 66045

Dengfeng Sun¶
Purdue University, West Lafayette, IN 47907

Tomoki Takegami‖
Mitsubishi Electric Corporation, Amagasaki City, Japan

The electrification of pneumatic or hydraulic system on aircraft has been shown effective in reducing the fuel burn. Recently, electrifying propulsive loads has attracted a lot of attention to further improve fuel economy. This work focuses on tools to facilitate more electric aircraft at conceptual design stage, particularly assuming a turbo-generator architecture. Specifically, we develop a simulation tool, mimicking SUAVE [1], which allows mission and fuel burn analysis. Major differences from SUAVE include more detailed models of components in the electric propulsive branch and degrees of freedom to adjust the velocity profile along the entire mission. Based on the simulator, this work further proposes to leverage a gradient-free optimization technique, which optimizes the optimal velocity profile along the entire mission to minimize fuel burn. Simulation results on two aircraft designs, a conventional Boeing 737-800 and NASA-STARC-ABL, verify the effectiveness of the proposed tools.

I. Nomenclature

γ	=	heat capacity ratio for air
Φ_d, Φ_q	=	fluxes in d- and q-axis
Ω	=	rotor speed
ω	=	voltage frequency $p\Omega$
Φ_{pm}	=	permanent magnet flux
i_d, i_q	=	current in d- and q-axis
u_d, u_q	=	voltage in d- and q-axis
L_d, L_q	=	inductance in d- and q-axis
p	=	number of pole pairs
R_s	=	winding resistance
J	=	rotor inertia
T_G	=	driving torque from the prime mover
L	=	lift

*Graduate Student, School of Aeronautics and Astronautics
†Research Scientist
‡Senior Principal Research Scientist
§Associate Professor, Department of Mechanical Engineering
¶Professor, School of Aeronautics and Astronautics
‖Researcher, Advanced Technology R&D Center

D	=	drag
α	=	angle of attack
μ	=	induced angle of attack
F_{sp}	=	specific thrust
I_{sp}	=	specific impulse
F	=	thrust
M_∞	=	freestream mach number
a_∞	=	speed of sound
v_∞	=	freestream velocity
$\dot{m}$	=	mass flow rate
T_t	=	stagnation temperature
P_t	=	stagnation pressure
h_t	=	stagnation enthalpy
W	=	work done by components
β	=	bypass ratio
f	=	fuel to air ratio

II. Introduction

Increased growth in environmental concerns has made it evident that substantial cuts in Greenhouse Gas (GHG) emissions from the transportation sector are needed. Constituting roughly 2.1% of total human-induced CO2 emissions, the aviation industry has been actively exploring advanced energy-efficient and sustainable solutions to diminish its detrimental impacts. Important progresses have been made in the past decades to move toward More Electric Aircraft (MEA) designs [2], the main idea of which is to electrify non-propulsive loads in aircraft as much as possible. The increased level of aircraft electrification is projected to bring in benefits such as higher efficiency, controllability and reconfigurability, while facilitating ease of maintenance procedures [3]. This set of advantages is easily translated into economic benefits.

Along with the electrification of non-propulsive loads, electrifying propulsive loads draws intensive attention to further address the sustainability concern. Different architectures for Electrified Aircraft Propulsion (EAP) systems have been proposed in the literature [4, 5], for various types of aircraft and missions. Turboelectric architectures are particularly attractive for mid/large commercial aircraft, which lead not only to potentially significant fuel burn reduction as a result of improved aerodynamics by facilitating flexible configuration, but also improved technology readiness level by avoiding low energy-density but heavy energy storage pack. For example, turboelectric propulsion systems readily enable highly energy-efficient configurations such as Boundary Layer Ingestion (BLI) and distributed propulsion [6].

In the BLI design, the jet and wake are located along the same axis, resulting in less noise and drag, and thus increasing the aircraft's energy efficiency [5]. Hence, a turboelectric architecture strikes a nice balance between fuel burn reduction, power/energy density, and technological readiness level, hence becoming one of the most attractive topologies for more electric powertrains in the short term [7].

A potential turboelectric propulsion system configuration involving AC generator, power electronics, electric motor, and BLI fan, is depicted in Fig. 1. Different types of components can be integrated to fulfill the functionality of the electric propulsion branch. AC power sources, such as a Field Controlled Synchronous Generator (FCSG) or a Permanent Magnet Synchronous Generator (PMSG), can be used as a generation unit. On the load side, synchronous reluctance machine, induction machine, or Permanent Magnet Synchronous Motor (PMSM), etc. can be used.

Other than exploring advanced future propulsion system configurations, another common way to investigate the potential of reducing greenhouse gas emissions for aircraft is to perform trajectory optimization. Aircraft trajectory optimization has been widely studied for decades [8–13]. In [8], Pargett et al. proposed a flight path optimization method that allows aircraft to perform various velocities during the cruise while holding the same altitude. The results show that at most 7% of fuel, saving can be reached. The paper used the "Breguet range equation," which assumes a constant lift-to-drag ratio leaving only the range and mass as dynamic variables. Similarly, Park et al. in [9], proposed another flight trajectory optimization method for aircraft in descent to minimize the environmental impact in the presence of wind. They assume that aircraft lift always equals its weight, and the thrust is modeled as a function of airspeed and altitude. The authors in [10] provided a trajectory optimization method based on existing waypoints, and showed effective results on fuel saving by using a wind forecast, an airspace structure, etc., with a simple aircraft point mass model. Similarly, in [11], Lindner et al. showed a case study results that 680kg fuel can be saved for

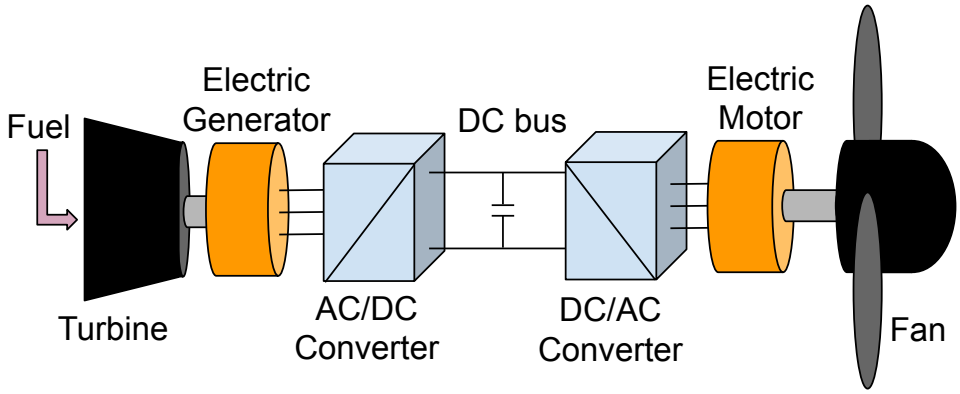

Fig. 1 General architecture example for a full turboelectric propulsion system.

a ~3500NM mission, Nairobi, Kenia (NBO) to Paris, France (CDG), by using trajectory optimization with utilized atmospheric parameters such as wind speed and wind direction. Those researchers have validated that through trajectory optimization, the improvement (reduction) in fuel consumption is significant. However, the lift and drag are nested with velocity, altitude, and weight changes along the mission to maintain a steady flight. This further results in various thrust requirements throughout the mission, therefore, impacting the total fuel burn. For this reason, we should not neglect the importance of formulating physical models for relative subjects when analyzing a long-haul mission.

In recent studies, the multidisciplinary aircraft design analysis with optimal trajectory optimization has been investigated by specifying specific aircraft system dynamic models. The relationship between the trajectory optimization results and the researchers' specific interests has been explored. For instance, Altus et al. in [12] performed a multidisciplinary optimization that described a simultaneous wing design and trajectory analysis using the Optimizer-Based Decomposition (OBD). The study revealed that the sizing of wing geometries and structures could lead to different predictions for minimum fuel and maximum rate climb, etc., thus affecting the overall mission profile optimization. Similarly, Falck et al. in [13], studied the effect of optimal trajectories on the thermal system constraints of an electric aircraft prototype. The study showed that optimal velocities satisfying thermal efficiencies did not conflict with the nominal optimal flight path in reducing energy consumption, as there are relatively minor deviations.

The studies mentioned above demonstrate the significant fuel savings achievable through trajectory optimization, and the value of multidisciplinary analysis in evaluating the impact of each subsystem at a system level. In this paper, our focus is on assessing the potential of the turboelectric concept with trajectory optimization for achieving carbon neutrality in the aviation industry. To this end, we utilized SUAVE [1], a state-of-the-art multidisciplinary conceptual level aircraft design environment, as a guide to develop a mission analysis tool. Our new process incorporates a multidisciplinary simulation framework, as well as more detailed models of components in the electric propulsive branch and degrees of freedom to adjust the velocity profile throughout the mission. In the simulation, we incorporated aerodynamic models that accommodate distinct wing configurations for different mission segments (climb, cruise, and descent), with modularized propulsion system dynamic models (including turbofan and ducted fan engines), and 0D dynamic models for the electric propulsion system (EPS), which are crucial for future electric aircraft design. We verified our mission analysis tool by using the Boeing 737-800 [14] aircraft as our baseline model, and a conceptual design proposed by NASA in [15]: the single-aisle turboelectric commercial transport with fuselage boundary layer ingestion (STARC-ABL), as a guideline for our future aircraft model. Finally, we employed a gradient-free optimization technique with modifications based on [16] to optimize the velocity profile along the entire mission and minimize fuel burn for both models.

The paper is organized as follows: Section III presents the mission requirements and a simplified 2D aircraft equations of motion. This section helps investigate the benefits of adjusting angle of attack (AoA), thrust, and velocity along the flight mission. Section IV describes the setups of aerodynamics, 0D propulsion network models, flight missions, and the architecture of the multidisciplinary mission analysis tool. In Section V, we describe a simulator-based gradient-free mission optimization that nests with our mission analysis tool and aircraft models. Section VI showcases the effectiveness of our mission analysis tool through case studies of the optimization results from the baseline and STARC-ABL. Finally, Section VII concludes our work and discusses our plan for future improvements.

III. Problem Formulation

At the conceptual design stage, the system designer determines an initial concept of aircraft configuration, geometry (fuselage, wing, tail, etc.), engine, landing gear, max takeoff weight, etc., based on customer requirements such as mission and economical cost. The mission requirements include max takeoff weight, travel time/distance, payload, altitude, etc. A common practice in aircraft flight mission analysis is to assume the aircraft flies at a constant speed during the cruise with a constant angle of attack (AoA) and a constant rate of altitude change during climb/descent. This treatment simplifies the aircraft operation and reduces the complexity of the resultant mission optimization problem, albeit at the expense of increased fuel burn, due to lack of flexibility. This work explores what freedom within the mission can be leveraged to reduce fuel burn and how to verify it in a trustworthy manner. Particularly, we investigate the benefits of adjusting the following parameters along the entire mission: the angle of attack, thrust, and velocity along the entire flight mission.

To strike the balance between the feasibility and computational burden during the conceptual design stage, it is realistic to only consider the aircraft statics in the 2-dimensional (xy) plane, where the horizontal (x) and vertical (y) axes represent the travel distance and the altitude of the aircraft, respectively. The corresponding free-body diagram is shown in Fig. 2, where L, D, F, and mg represent the lift, drag, thrust, and gravitational force, respectively. Additionally, α represents the AoA, μ the flight path angle, and θ the pitch angle. When treated as a point-mass, the aircraft is subject to the following force balance equation.

$$\begin{aligned} F\cos(\alpha+\mu) - D\cos\mu - L\sin\mu &= 0 \\ F\sin(\alpha+\mu) - D\sin\mu + L\cos\mu - mg &= 0. \end{aligned} \tag{1}$$

By assuming the aircraft as a point-mass, all forces are exerted on the center of mass and the momentum balance is ignored. Since the required thrust F is related to the aircraft's weight, and this weight is decreasing along the mission as the result of the amount of fuel consumed by the engine. Thus, (1) is time-varying along the mission.

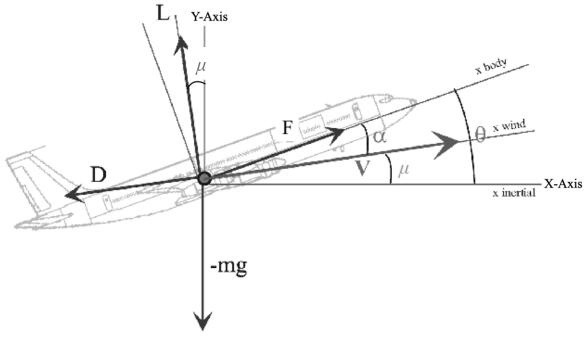

Fig. 2 Aircraft Point Mass Free-body Diagram [17].

The aircraft is subject to nonlinear algebraic constraints arising from mission completion:

$$\begin{aligned} \text{mission time: } & t_f \in [0, \bar{t}_f] \\ \text{mission distance: } & x(0) = 0, \quad x(t_f) = S_x \\ \text{fuel weight: } & m_f \in [0, \bar{m}_f] \\ \text{takeoff weight: } & m_w = m_0 + m_f + m_l \le M \\ \text{angle of attack: } & \alpha \in [\underline{\alpha}, \bar{\alpha}] \\ \text{velocity: } & v \in [\underline{v}, \bar{v}] \\ \text{engine thrust: } & F \in [\underline{F}, \bar{F}], \end{aligned} \tag{2}$$

where S_x is the required mission range, m_0 and m_l are the empty weight and payload, respectively, and M is the maximum takeoff weight. Given a dummy variable ξ the variables $\underline{\xi}$ and $\bar{\xi}$ denote lower and upper bounds of ξ,

respectively. Note that the upper and lower bounds are typically not constant over the entire mission. For instance, the lower and upper bounds of the velocity on the ground and at 10000ft altitude are different. Here we ignore their arguments for concise representation without causing confusion.

Constraints on most of the variables, such as m_f, α, v, F, have to be enforced over the entire mission. Constraints on some variables can be enforced over finite points, by considering simple facts. For example, m_w reaches its maximum at $t = 0$, and thus constraint $m_w \leq M$ is collapsed into $w_w(0) \leq M$. Also, it is evident that m_f is monotonically decreasing along the mission and reaches the minimum value at $t = t_f$. Thus the fuel weight constraint can be reduced to $m_f(t_f) \geq 0$, if zero reserve is assumed.

For mission optimization, it is natural to pick the fuel burn as the cost function. Let $\dot{m}_f(t)$ be the fuel burn rate at time t. Hence, we consider the cost function

$$J = \int_0^{t_f} \dot{m}_f(t)\mathrm{d}t. \tag{3}$$

With (1)–(3), we are ready to formulate the mission optimization problem as follows.

Problem III.1 *Given force balance formula* (1)*, mission description* (2)*, and cost function* (3)*, find the optimal solution to the following optimization problem:*

$$\min_{t_f, v\in\mathcal{U}, \alpha\in C_\alpha, F\in\mathcal{F}} J(v) \tag{4a}$$

s.t.

$$x(t_f) = \int_0^{t_f} v_x \mathrm{d}t = S_f \tag{4b}$$

$$y(t+\delta t) = y(t) + \int_t^{t+\delta t} v_y \mathrm{d}t \tag{4c}$$

$$g_i(v, \alpha, m, L, F, D, x, y) \leq 0 \tag{4d}$$

$$g_e(v, \alpha, m, L, F, D, x, y) = 0, \tag{4e}$$

where $\mathcal{U}$ is the space of continuous functions $v : [0, t_f] \to [\underline{v}, \bar{v}]$, C_α is the space of continuous function such that $\alpha : [t, t_f] \to [\underline{\alpha}, \bar{\alpha}]$, and $\mathcal{F}$ is the space of continuous function such that $F : [0, t_f] \to [\underline{F}, \bar{F}]$.

Note that v, α, F might not be free to choose while satisfying force balance constraint. The dimension of design freedom will be reduced to one. For the mission optimization of interest, this work considers Problem III.1 with decision variables being v only.

Remark III.2 *Function $g_i(\cdot)$ and $g_e(\cdot)$ are an abstraction of the constraints arising from aircraft physics, e.g. force balance equation, aerodynamics, turbofan engine, mission, airport class/region, and FAA regulations. The elements related to aerodynamics and turbofan engine can be obtained by re-arranging the aerodynamics and turbo-fan engine equations detailed in the Appendix. The expressions of components related to other factors can vary wildly though. Examples of mission and FAA regulation-related constraints can be found in Section IV.C.*

IV. System Modeling and Simulator

System modeling for Problem III.1 establishes the dependence of cost function and constraints on decision variables: how v, α, F in (1) are coupled with aircraft geometry and configuration through aerodynamics, with turbofan engine, fuel burn, generator voltage and power, motor voltage, power, etc, and with mission requirements. Here we sketch the key points of aerodynamics and turbofan engine while leaving most of details in the Appendix for self-completeness. This section is largely devoted to modeling the components of the electric propulsion branch. The simulation environment can be viewed as a modified version of SUAVE, with some extensions on enriching components of the electric propulsion branch.

A. Aerodynamics

Aerodynamics is the fundamental principle applied to quantify the aircraft lift force L and drag force D, for a given aircraft geometry, configuration and flight conditions. Both forces, directly affecting the propulsion system's

thrust, the power demand, and thus the fuel burn, are critical to mission analysis and performance. We resort to two approaches accounting for different levels of fidelity for aerodynamics. For lower fidelity, we take basic parametric aircraft geometries and perform the numerical approximation of aerodynamic parameters by using the vortex lattice method (VLM). For higher fidelity, given the complexity and the availability of mature software, we avoid calculations by using empirical equations. In this paper, we use the second method to generate the lookup tables for aerodynamics. Particularly, we rely on NASA's Open Vehicle Sketch Pad (OpenVSP) [18] to calculate aerodynamic properties offline, by running its built-in analysis tools, e.g., VSPAERO and Parasite Drag Analysis.

B. Propulsion

The modeling of propulsion systems boils down to modeling each component, such as turbofan engine, generator, cable, power electronics, electric machine, fan, etc. We present steady-state models of components suitable for both turbofan engine-based and turboelectric-based propulsion systems, as shown in Fig. 3. Inside the blue dash-dotted box is the block diagram of the conventional turbofan propulsion system. The turboelectric propulsion, motivated by the concept of STARC-ABL [15], contains the turbofan engine propulsion system and an electric propulsion branch, which is shown as the block diagram inside the red-dotted box. As depicted in Fig. 3, a certain amount of shaft power is drawn from the gas turbine and converted into electricity by the generator, which is further delivered to the rear fuselage fan through the electric propulsion network.

The modeling of turbofan engine modules, such as compression nozzle, fan, compressor, burner, turbine, and expansion nozzle, follows standard textbook methods attached in the Appendix [19]. The parameters used for CFM international's CFM56-7B24 engine are shown in [20, 21]. The components involved in the electric propulsion branch, such as the generator, inverter, converter, and motor, are modeled below. We first derive dynamic models and then obtain their steady-state counterparts.

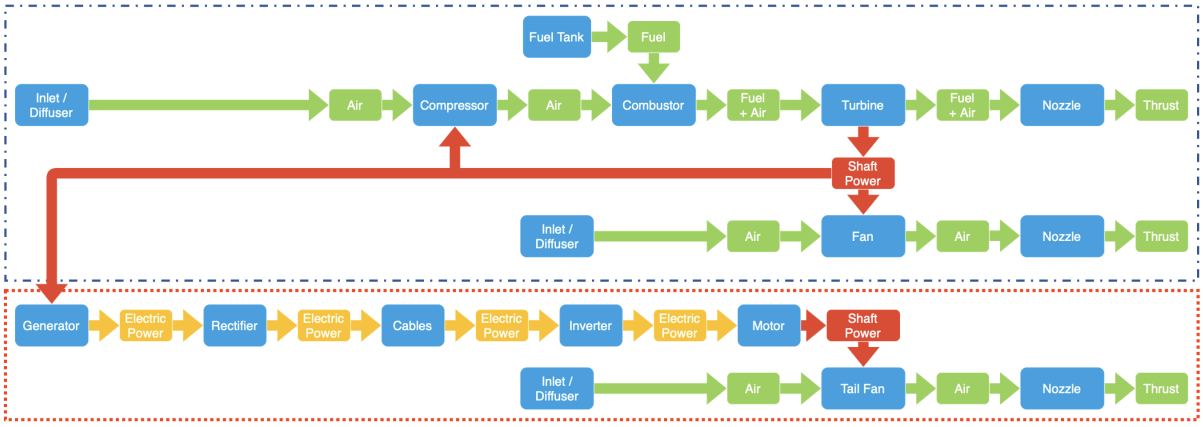

Fig. 3 Turboelectric Propulsion Network

1. Surface-mounted Permanent Magnet Synchronous Generator

A Surface-mounted Permanent Magnet Synchronous Generator (SPMSG) is used for converting shaft power into electricity. Its dynamics can be captured by the left equivalent circuit as shown in Fig. 4. The corresponding model is

given as follows

$$
\begin{aligned}
\dot{i}_d &= -\frac{1}{L_d}(R_s i_d + \omega\Phi_q + u_d) \\
\dot{i}_q &= -\frac{1}{L_q}(R_s i_q - \omega\Phi_d + u_q) \\
J\dot{\Omega} &= T_G - \frac{3p}{2}(i_q\Phi_d - i_d\Phi_q) \\
\Phi_d &= -L_d i_d + \Phi_{\text{pm}} \\
\Phi_q &= -L_q i_q \\
\omega &= p\Omega,
\end{aligned}
\tag{5}
$$

where $L_d = L_q$, T_G is the torque from the shaft, u_d, u_q are terminal voltages coupled with loads, the input power for the SPMSG generator is $P_{\text{gen,in}} = \frac{3}{2} i_q p \Phi_{\text{pm}} \Omega$, and the output power is $P_{\text{gen,out}} = \frac{3}{2}(u_q i_q + u_d i_d)$. Typically, $i_d = 0$, and thus the output power is $P_{\text{gen,out}} = \frac{3}{2} u_q i_q$.

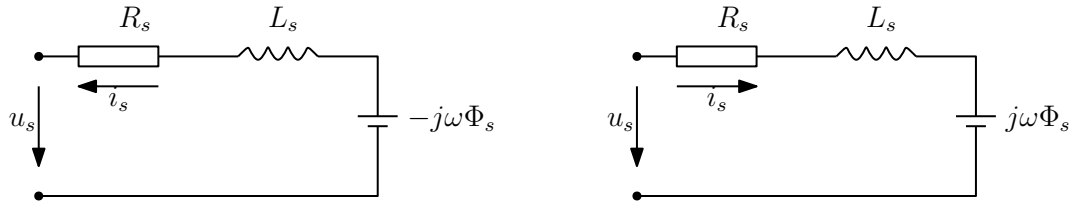

$j\omega\Phi_s + L_s\dot{i}_s + R_s i_s + u_s = 0$ $\qquad$ $R_s i_s + L_s\dot{i}_s + j\omega\Phi_s - u_s = 0$

Fig. 4 Equivalent circuits of SPMSG (left) and SPMSM (right).

2. Surface-mounted Permanent Magnet Synchronous Motor

A Surface-mounted Permanent Magnet Synchronous Motor (SPMSM) bridges the electric bus and the tail fan propulsor, transforming electric power to shaft power driving the tail fan. According to the right equivalent circuit in Fig. 4, the SPMSM model admits the following state-space representation

$$
\begin{aligned}
\dot{i}_d &= \frac{1}{L_s}(-R_s i_d + p\Omega L_s i_q + u_d) = -\gamma i_d + p\Omega i_q + \frac{u_d}{L_s} \\
\dot{i}_q &= \frac{1}{L_s}(-R_s i_q - (L_s i_d + \Phi_{\text{pm}}) p\Omega + u_q) = -\gamma i_q - p\Omega(i_d + \frac{\Phi_{\text{pm}}}{L_s}) + \frac{u_q}{L_s} \\
J\dot{\Omega} &= \frac{3p}{2}\Phi_{\text{pm}} i_q - T_L,
\end{aligned}
\tag{6}
$$

where $L_s = L_d = L_q$ and $\gamma = R_s/L_s$. At steady-state, the SPMSM motor input power required is $P_{\text{mot,in}} = \frac{3}{2}(i_d u_d + i_q u_q)$, where i_d is typically 0 at steady-state, and u_d, u_q, i_q can be determined by any given motor operation point at (Ω, T_L). The motor output power is $P_{\text{mot,out}} = \frac{3p}{2}\Phi_{\text{pm}} i_q \Omega$.

3. Converter & Inverter

For converter and inverter, we assume 99% efficiency for simplicity, and the inverter is directly connected with the converter since cables are not yet modeled. Thus, the input power required for the inverter and the converter becomes $P_{\text{inv,in}} = \frac{P_{\text{mot,in}}}{0.99}$ and $P_{\text{con,in}} = \frac{P_{\text{inv,in}}}{0.99}$.

4. Thrust & Fuel Consumption Rate

For the baseline aircraft B738, we derive the fuel consumption based on the thrust of the turbofan engine. For the STARC-ABL, we calculate the fuel consumption based on the thrusts corresponding to both the turbofan engine and

electric propulsion branch. Note that the electric propulsion thrust has been mapped into the mechanical power drawn from the shaft of low compressor turbine by the generator.

For B738, the turbofan engine model is used to construct the energy network as the power source to provide thrust. To calculate the turbofan thrust, stagnation quantities (e.g., stagnation temperature and pressure) are used to connect different components (e.g., compressor, burner, turbine, nozzle, etc.) and compute the engine's performance characteristics. Following Cantwell's method [19], the thrust can be calculated by equations (40)-(46). Further, The system's fuel flow rate (47) and engine power (48) can be observed based on the thrust specific fuel consumption (43) and the freestream velocity v_∞

For STARC-ABL, in addition to the turbofan energy network, a ducted fan energy network (which simulates the BLI propulsor) is added to the system. Together, they form the turboelectric energy network. To calculate the thrust from the ducted fan, we assumed that the structure of the ducted fan is similar to the bypass fan on the turbofan engine. Furthermore, we modified several engine parameters given in [15]. For example, the thrust flow constant becomes $C_{\text{core}} = 0$ and $C_{\text{fan}} = 1$ as there's no core thruster in the ducted fan engine. Thus, in (41), the core nondimensional thrust is set to $F_{\text{nd,core}} = 0$, and the fan nondimensional thrust is set to $F_{\text{nd,BLIfan}} = F_{\text{nd,fan}}$. Then, we can use the following equations for thrust and power calculation for the ducted fan:
Specific thrust & specific impulse

$$F_{\text{sp,BLIfan}} = \left(\frac{1}{\gamma M_\infty}\right) F_{\text{nd,BLIfan}} \tag{7}$$

Fan mass flow rate

(fan flow sizing)

$$\begin{aligned} \dot{m}_{\text{size,BLIfan}} &= \frac{F_{\text{design,BLIfan}}}{F_{\text{sp,BLIfan}} a_\infty} \\ \dot{m}_{\text{nd,BLIfan}} &= \frac{\dot{m}_{\text{size,BLIfan}}}{\sqrt{\frac{T_{\text{ref}}}{T_{t5,\text{ground}}}} \left[\frac{P_{t5,\text{ground}}}{P_{\text{ref}}}\right]} \end{aligned} \tag{8}$$

(fan mass flow)

$$\dot{m}_{fan} = \frac{\dot{m}_{\text{nd,BLIfan}}}{\sqrt{\frac{T_{\text{ref}}}{T_{t5}}} \left[\frac{P_{t5}}{P_{\text{ref}}}\right]} \tag{9}$$

Thrust (2-Dimensional):

$$F_{\text{BLIfan}} = F_{\text{sp,BLIfan}} \cdot a_\infty \cdot \dot{m}_{\text{BLIfan}} \cdot \eta_{\text{throttle,BLIfan}} \tag{10}$$

BLI fan power

$$\text{Power} = F_{\text{BLIfan}} \cdot v_\infty \tag{11}$$

Where a_∞ is the speed of sound, v_∞ is the free stream velocity, $g = 9.81 m/s^2$ is the gravity of earth, T_{t5} is the turbine exit stagnation temperature, P_{t5} is the turbine exit stagnation pressure, η_{throttle} is the throttle setting at each control point, $T_{\text{ref}} = 288.15$ K is the reference temperature, and $P_{\text{ref}} = 101.325$ kPa is the reference pressure. Like the turbofan engine, in (8) we use parameters from [15] for the BIL fan to evaluate its compressor nondimensional mass flow $\dot{m}_{\text{nd,BLIfan}}$, so that we can calculate the BLI fan's mass flow at different working conditions (e.g., at given altitude and freestream velocity followed by the mission setup) for its thrust calculation. Below is the diagram (Fig. 5) that expresses the thrust sizing process of the engine.

Combining the above equations for both turbofan and ducted fan engines, the total thrust of the turboelectric energy network is simply the sum of two turbofan engines and the ducted tail fan:

$$F_{\text{total}} = F_{\text{turbofan}} + F_{\text{BLIfan}} \tag{12}$$

To calculate the fuel consumption rate of the turboelectric energy network, recall that in Fig. 3, for EPS, the power extracted from the turbine shaft adds additional work to the turbine. Thus, for turbofan engines on STARC-ABL, Δh_{t5}, the enthalpy changes in the low pressure turbine (34), now includes the generator power W_{gen}:

$$\Delta h_{t5} = -\frac{W_{\text{lpc}} + \beta W_{\text{fan}} + W_{\text{gen}}}{(1+f)\,\eta_{\text{mech}}} \tag{13}$$

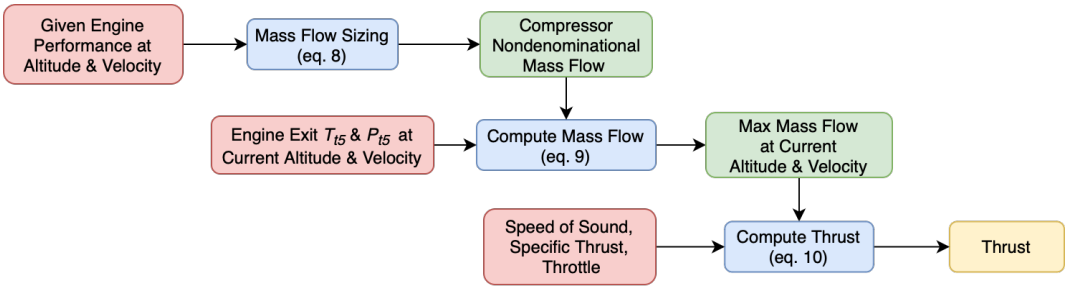

Fig. 5 Engine Sizing Process for both Turbofans and Ducted Fans.

This change further affects the stagnation quantities at the nozzle exit of the turbofan engine. In the end, combined with the additional thrust from the BLI fan, the fuel flow rate of the turboelectric system can be rewritten as the following equations:

Engine nondimensional thrust

$$F_{\text{nd,total}} = F_{\text{nd,turbofan}} + F_{\text{nd,BLIfan}} \tag{14}$$

Specific thrust & specific impulse

$$\begin{aligned} F_{\text{sp}} &= \left(\frac{1}{\gamma M_\infty}\right) F_{\text{nd,turbofan}} \\ I_{\text{sp}} &= F_{\text{sp}} \cdot a_\infty \frac{1+\beta}{fg} \end{aligned} \tag{15}$$

Thrust specific fuel consumption

$$\text{TSFC} = \frac{1}{I_{\text{sp}}} \left(1 - \text{SFC}_{\text{adj}}\right) \cdot hr \tag{16}$$

Fuel flow rate

$$\dot{m}_f = F_{\text{total}} \frac{\text{TSFC}}{g} \tag{17}$$

where SFC_{adj} is the adjustment parameter for the specific fuel consumption.

C. Mission

An aircraft flight mission can be divided into different phases, for example, climb, cruise and descent. Each phase can be further divided into multiple segments separated by altitudes due to velocity limitations based on operating safety and airspace regulations, wing configurations, as well as introducing degrees of design freedom. In addition, in our mission analysis, we further discretized each of those segments with a fixed number of sub-segments and evaluated the propulsion system at the initial point of those sub-segments, which we call control points. Besides, for the initial mission setup, in climb and descent, each sub-segment is defined with a constant rate of climb/descent and with a constant airspeed. For the cruise phase, the aircraft is operating at a constant altitude and its velocity is constant within the sub-segments. The velocities within the sub-segments are subject to modification through the optimization process. Furthermore, aircraft wing configurations at different sub-segments are another important feature that we considered in the mission. Thus, flaps and slats settings are also specified for each sub-segment. For example, a typical Boeing 737-800 flight mission profile can be defined as shown in Fig. 6, we assume the aircraft takes off and lands at the airport with class B, C, or D airspace.

Consider the first climb segment as an example for sub-segments. In this stage, since the aircraft is taking off from controlled airspace (Class B, C, or D), the velocity of the aircraft is limited to no more than 200 knots based on regulations stated in FAA § 91.117 [22]. In addition, the AoA has to be between -10° and 10°, since the VLM method we used for aerodynamic calculation does not provide a good estimation when the AoA is large. Mean while the aircraft wings are positioned at flap 5 and slat 1 for takeoff configuration. Thus, the constraint function for this particular segment can be written as follows:

$$\text{airspeed: } 0 \le v \le 200 \text{ knots} \tag{18a}$$

$$\text{angle of attack: } -10^\circ \le \alpha \le 10^\circ \tag{18b}$$

$$\text{aircraft mass: } m_{empty} \leq m \leq m_{takeoff} \tag{18c}$$

$$\text{lift (with corresponding airspeed): } L_{\alpha=-10^\circ} \leq L \leq L_{\alpha=10^\circ} \tag{18d}$$

$$\text{drag (with corresponding airspeed): } D_{\alpha=-10^\circ} \leq D \leq D_{\alpha=10^\circ} \tag{18e}$$

$$\text{engine thrust: } 0 \leq F \leq F_{max} \tag{18f}$$

$$\text{Altitude: } 0 \leq y \leq 1500 \text{ ft} \tag{18g}$$

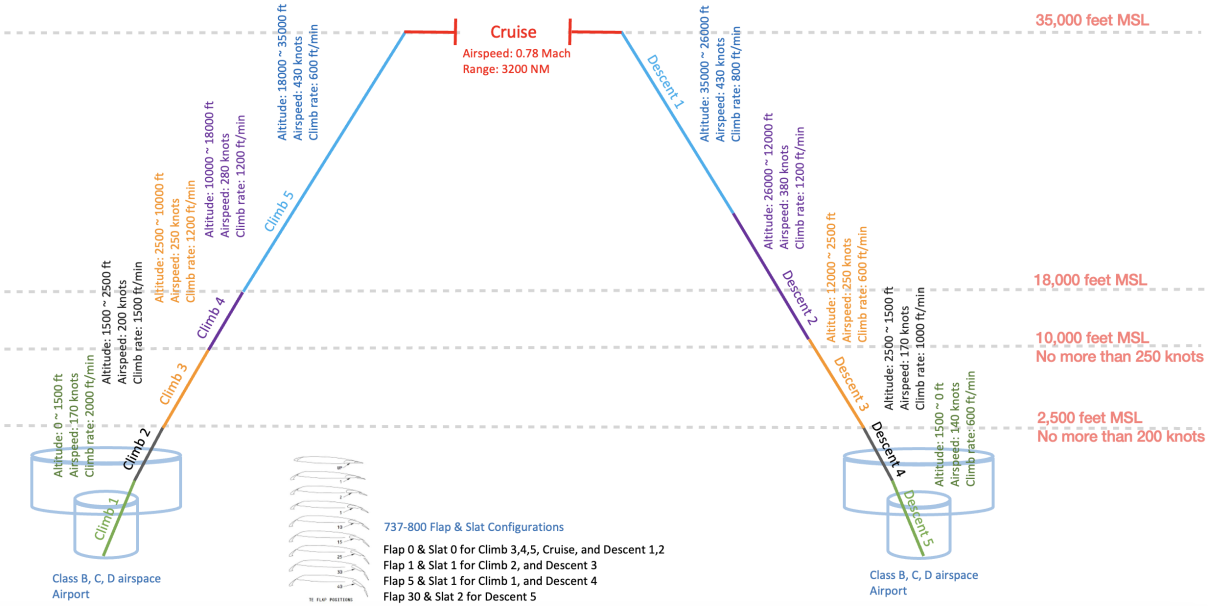

Fig. 6 Boeing 737-800 Flight Mission Profile Setup

D. Simulator

Given the models of aerodynamics and the propulsion system, we implement a simulator which takes velocity (along horizontal and vertical directions) and altitude as input and spits out fuel burn as its output. The simulator can also take a velocity vector of the entire mission as an input for mission analysis and optimization.

1. Architecture

In our mission analysis tool, we improved the architecture of SUAVE to meet our specific needs. For example, we generated aerodynamic results beforehand and stored them as lookup tables. Meanwhile, we pre-calculated the engine's performance characteristics before solving the force balance equations to speed up the analysis process. Additionally, we enhanced the aircraft's energy system components by constructing dynamic models for the EPS branch and enabling distributed thrust control from different propulsion systems to improve the simulation's fidelity. Below, we offer an overview consisting of three parts for self-completeness.

1) Aircraft and Flight Mission Setup, as shown in Fig. 7.
2) Mission Analysis, as shown in Fig. 8.
3) Results Collection, as shown in Fig. 8.

The functionality of Result Collection is self-explanatory, and thus omitted. Below we mainly explain the first two parts.

2. Aircraft and Flight Mission Setup

As shown in Fig. 7, the aircraft and flight mission setup defines: a) Vehicle, which specifies the aircraft geometry and configurations, propulsion system, and takeoff/empty/fuel weight of the aircraft; b) Mission Profile, including speed, range, and altitude information at individual segment; c) Settings, specifying the number of steady state control points, initial velocity at each control points, and methods of calculation for mission analysis.

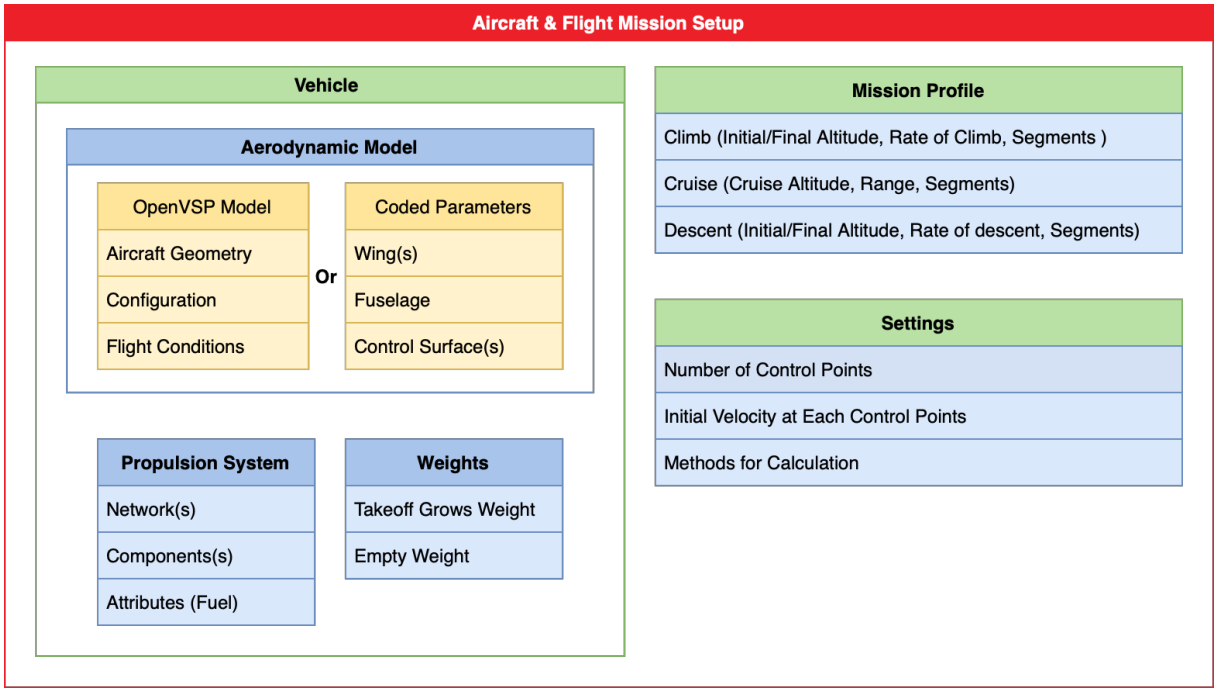

Fig. 7 Aircraft and Flight Mission Setup

3. Mission Analysis

As shown in Fig. 8, mission analysis first evaluates the aerodynamic parameters, force balance equation and propulsion system characteristics based on the vehicle and mission profile setting. Notice that this evaluation will be performed at each given control point until the mission finished.

Mission analysis performs steady-state analysis at each control point (control point and sub-segment are used interchangeably) where the total number of control points are predefined in the analysis settings. At each control point (each sub-segment), the aircraft is:

1) Climbing with a constant speed and rate.
2) Cruising with a constant speed and altitude.
3) Descending with a constant speed and rate.

Thus, the flight dynamics involve zero acceleration (The transient of velocity can be taken into account and is left for future work). The corresponding force balancing equations for climb and descent are the same as (1). For the cruise segment, however, the altitude y is constant. Hence, $\mu = 0$ and $\alpha = \theta$ in Fig. 2. The drag D, which includes the breakdown component of lift induced drag $L \sin(\alpha_i)$, is horizontal and aligned with the negative x-axis. Therefore, the force balancing equation is given by (1) with $\mu = 0$.

By solving for required thrust F at each control point from the force balance equation, fuel flow rate can be then calculated by the method described previously for propulsion. Thus the total fuel burn for the ith control point can be calculated as follow:

$$m_{f_i} = \dot{m}_{f_i} \frac{y_f - y_i}{v_{y,i}}, \qquad \text{(Climb \& Descent)}$$

$$m_{f_i} = \dot{m}_{f_i} \frac{R_{\text{cruise}}}{k}, \qquad \text{(Cruise)}$$

where $\dot{m}_{f_i}$ is the fuel flow rate at the ith control point, y_i and y_f are the initial and final altitude of the ith control point (sub-segment), $v_{y,i}$ is the rate of altitude change for the ith sub-segment, R_{cruise} is the cruising range, and k is the total number of control points defined for the cruise segment. Therefore, the total fuel burn of the mission becomes:

$$m_f = \sum_i m_{f_i} \tag{19}$$

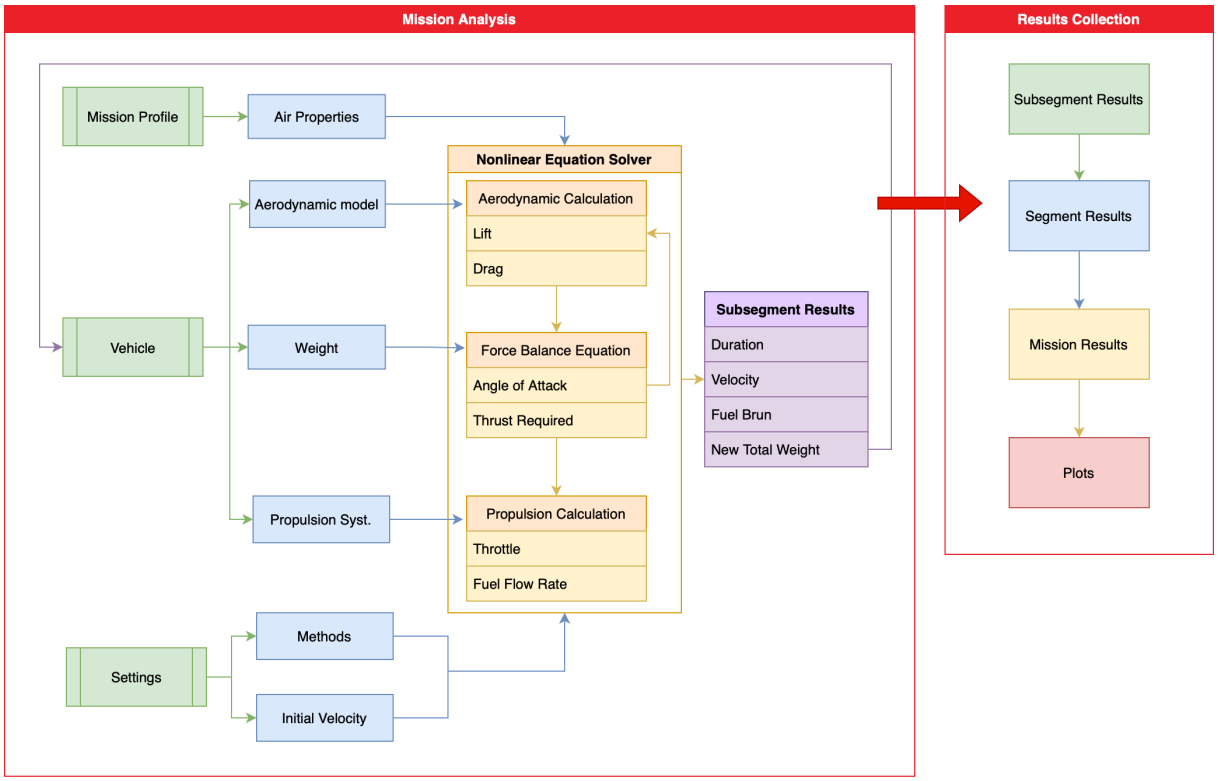

Fig. 8 Mission Analysis and Results Collection

V. Simulator-based Mission Optimization

Simulator involves aerodynamics and turbofan engine whose models admit the form of lookup tables, and thus the mapping that simulator implements in the current form, from its input to output, is non-differentiable. This section presents a gradient-free method to perform simulator-based mission optimization.

A. Mission Optimization Problem

Problem III.1 is presented in a form that the decision variables are continuous functions of travel distance x or time t. This ends up with an undesirable infinite-dimensional optimization problem. We first discretize the models and decision variables along the mission. Let's assume that climbing, cruising and descending are divided into N sub-segments, where the variable with subscript i denotes the variable at the ith sub-segment, for $1 \leq i \leq N$. For example, v_i denotes the velocity at the ith sub-segment. Aggregating variables of all sub-segments gives a vector. For example, all v_i for $1 \leq i \leq N$ are aggregated into a vector $V = [v_1, \cdots, v_N]^\top$.

We allow the aircraft have different but close speeds assigned at distinctive sub-segments. Therefore, for example, at the ith sub-segment during cruise, constraint function $g(\cdot)$ takes the form as follows

$$
\begin{aligned}
L_i &= f(v_i, \alpha_i, y_{\text{cruise}}) && \text{(20a)}\\
D_i &= f(v_i, \alpha_i, y_{\text{cruise}}) && \text{(20b)}\\
F_i &= f(v_i, y_{\text{cruise}}) && \text{(20c)}\\
\text{s. t. } v_i &\in [\underline{v}_i, \bar{v}_i] && \text{(20d)}\\
\alpha_i &\in [\underline{\alpha}, \bar{\alpha}] && \text{(20e)}\\
y_{\text{cruise}} &= 35000\ ft, && \text{(20f)}
\end{aligned}
$$

where $\underline{v}_i, \bar{v}_i$ represent the lower and upper bounds of velocity at the ith sub-segment, respectively.

B. Mission Optimizer

The following outlines how a simulation model can be used for mission optimization. In particular, it shows how to utilize evaluations of the simulation model without needing gradients in order to optimize Problem III.1. We use a modified version of the algorithm proposed in [16], where simulations of a digital twin are utilized for optimization. The modifications are due to the constraints on the traveled distance and velocity limits as discussed below. Notably, the algorithm does not require gradients making it appealing for the application to mission optimization, where gradients may be difficult and time-consuming to compute. Instead, the algorithm in [16] uses a simulation model as a black box, in which inputs to the simulation model (here, the velocity profile) generate a performance metric (here, the fuel consumption). The algorithm in [16] interprets an optimization problem as a stochastic estimation problem, in which the cost function induces a distribution for the inputs of the simulation model. Resulting from this interpretation, the optimization problem can be solved iteratively, where the iterations relate to recursions of the estimator. In [16], an Unscented Kalman Filter (UKF) is utilized, because it does not require gradients for optimization but only evaluations of so-called "sigma points". In our case, the sigma points describe a velocity profile to be tested by means of the simulation model. Hence, the algorithm uses the following main steps in each iteration k (with more detail in [16]):

1) Generate $N_{\text{sp}} = 2N + 1$ sigma points $V^{\text{sp}\ j} = \begin{bmatrix} v_1^{\text{sp}\ j} & \dots & v_i^{\text{sp}\ j} & \dots & v_N^{\text{sp}\ j} \end{bmatrix}^T$ with $j = 1, ..., 2N + 1$ from the current optimizer $V_k^\star$ and its distribution, where N is number of sub-segments in the mission.
2) Evaluate performance of $n_{\text{sp}} = 2n + 1$ sigma points with simulation model, i.e., compute fuel consumption for the flight mission.
3) Update optimizer $V_{k+1}^\star$ and its distribution using sigma points and their evaluations in order to initialize next iteration.
4) Evaluate stopping criterion of algorithm, e.g., fuel consumption of the mission defined by $V_{k+1}^\star$ improved by less than 0.01% compared to the mission defined by $V_k^\star$.

Remark V.1 *The UKF-based algorithm provides a framework for the systematic determination of sigma points, i.e., which simulations should be performed, and also a systematic way of using the results of such simulations to advance the optimizer for the next iteration(s). Further, by tracking not only the optimizer but also its distribution, the algorithm can converge faster, because the correlation between the different velocities is considered. This combination makes the algorithm quick to converge and easy to implement for optimization tasks, where only a simulation model is given.*

Constraints in the optimizer

Constraint on Traveled Distance In order to compare results of fuel consumption, the traveled distance during the mission needs to fixed. Note that we do not fix travel time, i.e., the optimizer is allowed to use travel time as a degree of freedom in order to optimize fuel consumption. During cruise, the simulation model uses a fixed distance constraint, i.e., the optimizer does not need to enforce additional constraints. However, during climb and descent, the simulation model uses a fixed time-constraint. This is mainly due to the fact that the mission phases during climb and descent are defined based on a fixed climb/descent rate in combination with altitude. Hence, in order to obtain the same traveled distance, we modify the optimizer to include an "average velocity" constraint. This way, not only the time is fixed, but also the traveled distance.

Constraint on Velocities In order to enforce limits on the velocities during the various phases, we introduce inequality constraints. These inequality constraints are used to make the flight mission adhere to user-specified constraints such as the ones displayed in Fig. 6.

VI. Case Studies

This section showcases the effectiveness of the proposed tools for the mission analysis and optimization by running two case studies. Fig. 9 shows the aerodynamic geometries we used in OpenVSP for Boeing 737-800 as the baseline based on publicly available data [23], and the turboelectric aircraft based on NASA's STARC-ABL conceptual design [15] for comparison. High lift devices such as flaps and slats are angled to the equivalent Flap 0, 1, 5, 30 and Slat 0, 1 positions for aircraft takeoff, cruise, and landing configurations [24].

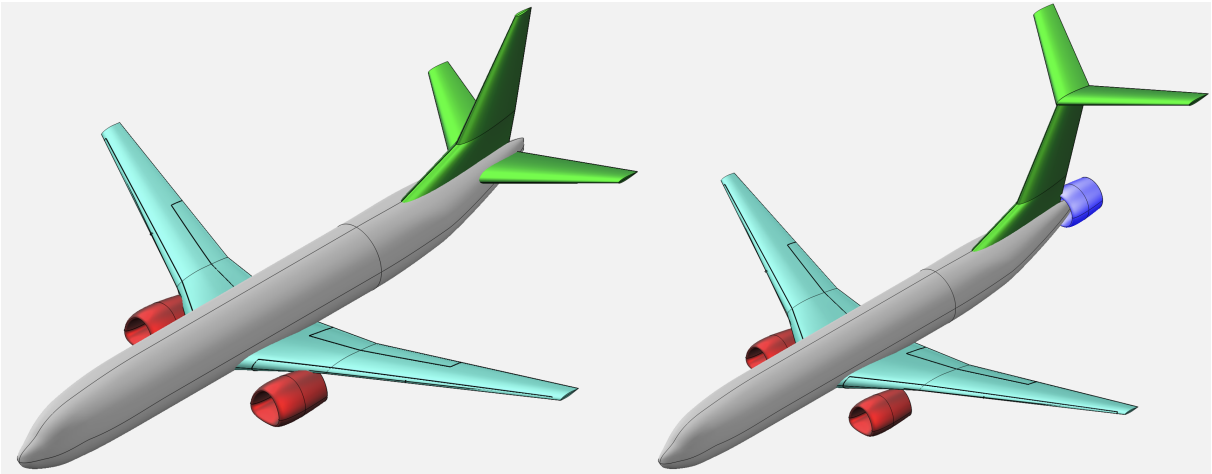

Fig. 9 Boeing 737-800 (Left) and STARC-ABL (Right) Models in OpenVSP

A. B737-800

Fig. 10 shows the mission optimization result for the first 150 iterations of the algorithm, where the velocity profile during climb, cruise, and descent is available to be adjusted to minimize the fuel burn. Here we divide the mission into total of 60 sub-segments, where the cruise segment was divided into 30 sub-segment and the climb and the descent segments are divided each into 3 sub-segments. During cruise, it can be observed that the optimal solution tends to start with higher speed and gradually decrease toward the end of cruise segment. This behavior will lead to more fuel burn in the beginning of the cruise phase, and consequently, the aircraft becomes lighter more quickly. During climb, it can be seen that the last sub-segment, i.e., the very last sub-segment before cruise increases. Note that we utilize the total distance constraint during climb and descent. Consequently, increasing the velocity in one sub-segment necessarily implies decreasing velocities in other segments. Fig. 10 shows that the optimizer chooses to increase the last sub-segment of climb 5. The reason for this observation is related to the altitude that the aircraft has reached in this sub-segment, which makes the aircraft more efficient. Fuel savings for the entire mission of using such an optimized velocity profile compared to the initial velocity profile are 2.69%.

B. STARC-ABL

Fig. 11 shows the mission optimization results for 200 iterations of the algorithm. Notice that the velocity profiles have a similar trend as shown in Fig. 10 due to the same reason described in the previous sub-section (e.g., it tends to start with a higher speed and gradually decreases toward the end of the cruise segment). However, the major difference is that the overall cruise velocity profile for STARC-ABL is slower than the one for B737-800, between 0.71 to 0.77 Mach. One possible reason is that since the EPS is more efficient and constantly works on 100% power during the cruise, thus reaching higher velocities requires the turbofan engines to produce more thrust as a compensation for increasing of drag. Consequently, it is better to cruise at lower velocities to increase the ratio between thrust from EPS to the turbofan engines so that the overall efficiency of the propulsion system can be higher. Consequently, fuel savings for the entire mission of using the optimized velocity profile compared to the initial velocity profile are 2.65%.

VII. Conclusions

This study created a multidisciplinary simulation environment for analyzing aircraft missions. A gradient-free method was utilized for optimizing missions based on simulations. The study demonstrated that optimizing aircraft trajectories, with either conventional turbofan engine propulsion or turboelectric propulsion systems, leads to an intuitive mission profile that satisfies constraints and provides fuel-saving benefits. The findings also showed that More Electric Aircraft (MEA) configurations may require slower optimal velocities in the mission profile than conventional aircraft because of the need to maximize the thrust portion from EPS so that the system can hold higher propulsive efficiency along the flight.

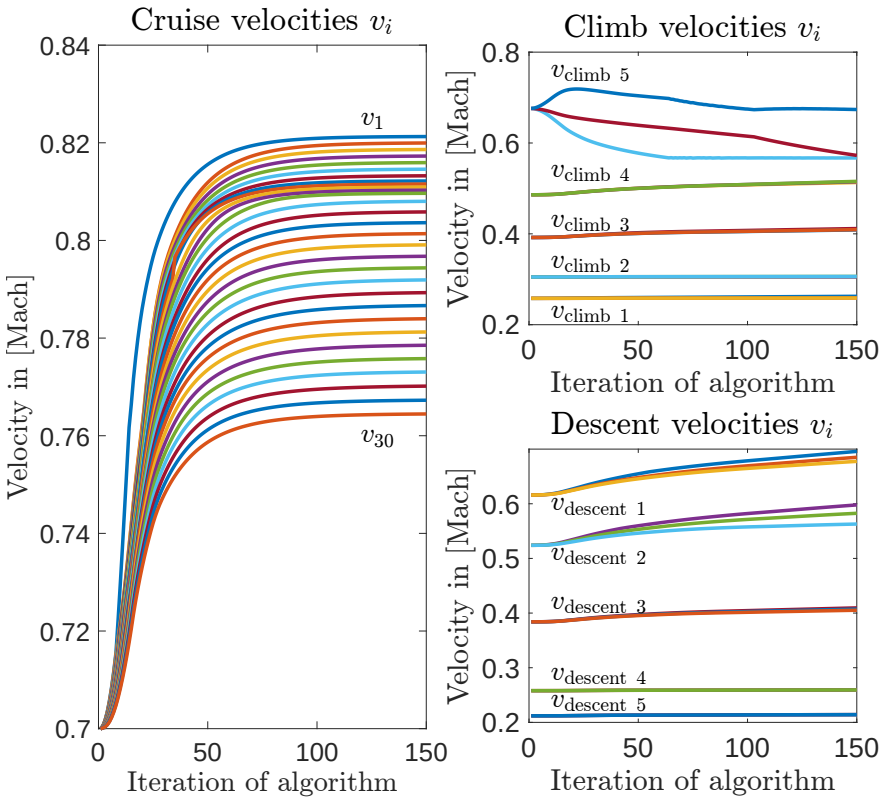

Fig. 10 Boeing 737-800: mission profile optimization result

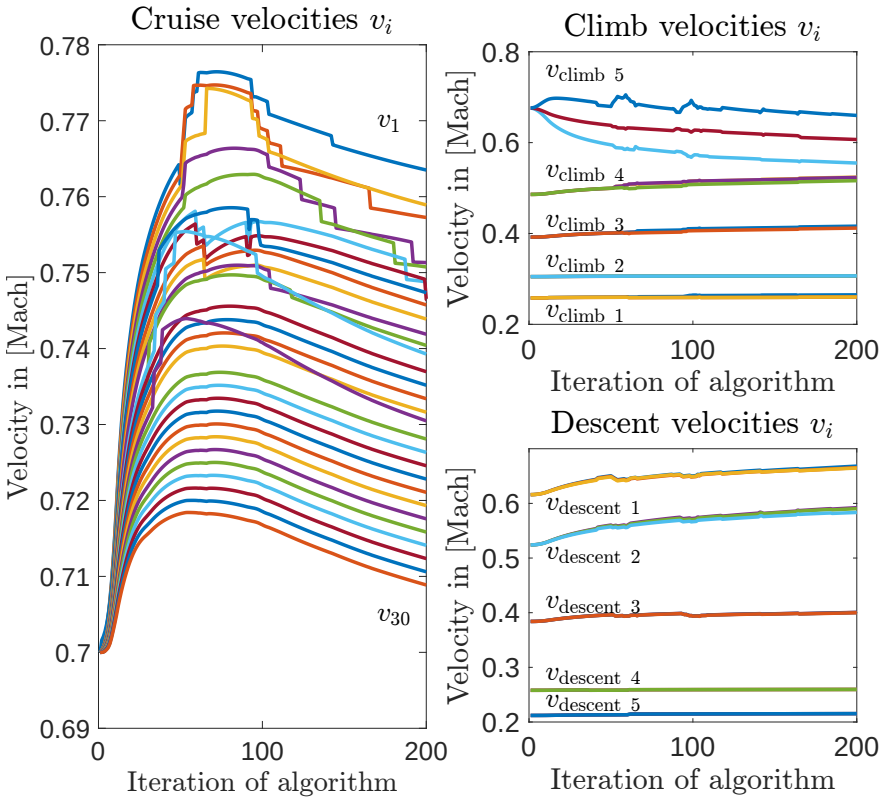

Fig. 11 STARC-ABL: mission profile optimization result

Appendix

A. Turbofan-engine

We describe how the thrust and mass flow are calculated through each component follows standard textbook methods from [19]. A typical commercial turbofan engine as shown in the Fig. 12 is used as an example, where the parameters are based on the CFM56-7B24 engine [21]:

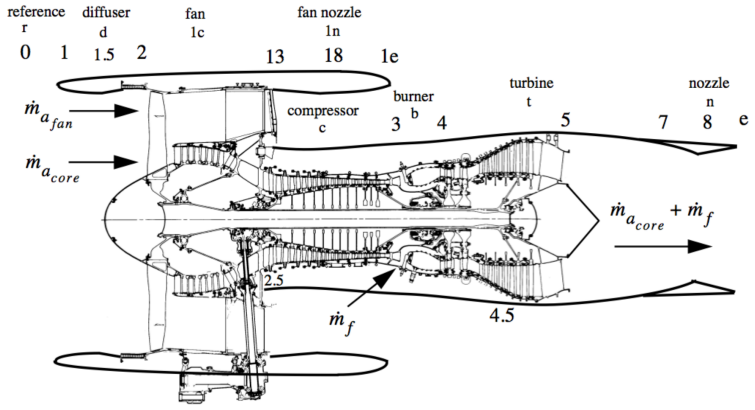

Fig. 12 Notation for Typical Commercial Turbofan Engine [25]

1. Station 0, Upstream State Conditions

The upstream stagnation temperature $T_{t0} = T_{t\infty}$, and pressure $P_{t0} = P_{t\infty}$ are calculated by: the free stream Mach number M_∞, static temperature $T_0 = T_\infty$, static pressure $P_0 = P_\infty$, and specific heat ratio for air γ.

$$\begin{aligned} T_{t0} &= \mathrm{T}_0 \left[1 + \left(\frac{\gamma - 1}{2}\right) M_\infty^2\right] \\ P_{t0} &= P_0 \left[1 + \left(\frac{\gamma - 1}{2}\right) M_\infty^2\right]^{\frac{\gamma}{\gamma - 1}} \end{aligned} \tag{21}$$

2. Station 1-2, Diffuser or Inlet Nozzle

This subsection calculates the output conditions of diffuser or inlet nozzle, also known as compression nozzle. Assuming the engine configuration is given, that is, pressure ratio f, the specific heat C_p for air at constant pressure, and the polytropic efficiency η. The outputs are stagnation quantities, velocity, and enthalpy.

Input conditions:

$$\begin{aligned} T_{t1} &= T_{t0} \\ P_{t1} &= P_{t0} \end{aligned} \tag{22}$$

Output stagnation quantities:

$$\begin{aligned} P_{t2} &= P_{t1} \cdot \pi \\ T_{t2} &= T_{t1} \cdot \pi^{\frac{\gamma-1}{\gamma} \cdot \frac{1}{\eta_{\text{nozzle}}}} \\ h_{t2} &= C_p T_{t2} \end{aligned} \tag{23}$$

Exit velocity and enthalpy:

$$\begin{aligned} h_2 &= C_p T_2 \\ u_2 &= \sqrt{2\left(h_{t2} - h_2\right)} \end{aligned} \tag{24}$$

3. Low & High Pressure Compressor

This subsection calculates the output conditions for both low and high pressure compressors. To drive those compressors, the work is taken out from turbines and delivered as shaft power. Again, assuming the engine configuration is given, that is, pressure ratio π, the specific heat C_p for air at constant pressure, and the polytropic efficiency η. The outputs are stagnation quantities, velocity, and enthalpy h in $[J/kg]$.

Output stagnation quantities:

(LPC)

$$\begin{aligned} P_{t2.5} &= P_{t2} \cdot \pi \\ T_{t2.5} &= T_{t2} \cdot \pi^{\frac{\gamma-1}{\gamma} \cdot \frac{1}{\eta_{\text{compressor}}}} \\ h_{t2.5} &= C_p T_{t2.5} \end{aligned} \tag{25}$$

(HPC)

$$\begin{aligned} P_{t3} &= P_{t2.5} \cdot \pi \\ T_{t3} &= T_{t2.5} \cdot \pi^{\frac{\gamma-1}{\gamma} \cdot \frac{1}{\eta_{\text{compressor}}}} \\ h_{t3} &= C_p T_{t3} \end{aligned} \tag{26}$$

Work done by compressor:

(LPC)

$$W_{\text{lpc}} = h_{t2.5} - h_{t2} \tag{27}$$

(HPC)

$$W_{\text{hpc}} = h_{t3} - h_{t2.5} \tag{28}$$

4. Fan

This subsection calculates the output conditions of the bypass stream through the fan. To drive the fan, the work is taken out from low pressure turbine and delivered as shaft power. Again, assuming the engine configuration is given, that is, pressure ratio π, the specific heat C_p for air at constant pressure, and the polytropic efficiency η. The outputs are stagnation quantities, velocity, and enthalpy h in $[J/kg]$.

Output stagnation quantities:

$$\begin{aligned} P_{t13} &= P_{t2} \cdot \pi \\ T_{t13} &= T_{t2} \cdot \pi^{\frac{\gamma-1}{\gamma} \cdot \frac{1}{\eta_{\text{fan}}}} \\ h_{t13} &= C_p T_{t13} \end{aligned} \tag{29}$$

Work done by fan:

$$W_{\text{fan}} = h_{t13} - h_{t2} \tag{30}$$

5. Burner

This subsection calculates the output conditions of the burner or also known as combustor. Here we assume the engine configuration is given, that is, pressure ratio π_b, the burner efficiency η_b, fuel specific energy $e_{t,Jet(A)}$, and the high pressure turbine inlet temperature T_{t4}.

Output stagnation quantities:

$$\begin{aligned} P_{t4} &= P_{t3} \cdot \pi_b \\ T_{t4} &= 1450\ K \text{ (B738 Only)} \\ h_{t4} &= C_p T_{t4} \end{aligned} \tag{31}$$

Fuel to air ratio:

$$f = \frac{h_{t4} - h_{t3}}{\eta_b e_{t,\text{Jet(A)}} - h_{t4}} \tag{32}$$

6. Low & High Pressure Turbine

This subsection calculates the output conditions for both low and high pressure turbines. In addition, the shaft power produced to drive both the fan and compressors. Again, assuming the engine configuration is given, that is, pressure ratio π, the specific heat C_p for air at constant pressure, mechanical efficiency η_{mech}, and the polytropic efficiency η_{pol}. The outputs are stagnation quantities, velocity, and enthalpy h in $[J/kg]$.

Energy across turbines:

(HPT)

$$\Delta h_{t4.5} = -\frac{W_{\text{hpc}}}{(1+f)\,\eta_{\text{mech}}} \tag{33}$$

(LPT)

$$\Delta h_{t5} = -\frac{W_{\text{lpc}} + \beta W_{\text{fan}}}{(1+f)\,\eta_{\text{mech}}} \tag{34}$$

Output stagnation quantities:

(HPT)

$$\begin{aligned} T_{t4.5} &= T_{t4} + \frac{t4.5}{C_p} \\ P_{t4.5} &= P_{t4}\left[\frac{T_{t4.5}}{T_{t4}}\right]^{\frac{\gamma}{(\gamma-1)\eta_{\text{pol}}}} \\ h_{t4.5} &= C_p * T_{t4.5} \end{aligned} \tag{35}$$

(LPT)

$$\begin{aligned} T_{t5} &= T_{t4.5} + \frac{t5}{C_p} \\ P_{t5} &= P_{t4.5}\left[\frac{T_{t5}}{T_{t4.5}}\right]^{\frac{\gamma}{(\gamma-1)\eta_{\text{pol}}}} \\ h_{t5} &= C_p * T_{t5} \end{aligned} \tag{36}$$

7. Expansion Nozzle

This subsection calculates the output conditions of The expansion nozzles, in our case, for both fan nozzle and core nozzle. Assuming the engine configuration is given, that is, pressure ratio f, the specific heat C_p for air at constant pressure, gas specific constant R, and the polytropic efficiency η_{EP}. The outputs are stagnation quantities, velocity, and enthalpy.

Output stagnation quantities:

$$\begin{aligned} P_{t,e} &= P_{t5} \cdot \pi \\ T_{t,e} &= T_{t5} \cdot \pi^{\frac{\gamma-1}{\gamma}\cdot\eta_{\text{EP}}} \\ h_{t,e} &= C_p T_{t,e} \end{aligned} \tag{37}$$

Output mach, velocity and static quantities:

$$\begin{aligned} M_e &= \sqrt{\left(\left[\frac{P_{t,e}}{P_0}\right]^{\frac{\gamma-1}{\gamma}} - 1\right)\frac{2}{\gamma-1}} \\ P_e &= P_0 \\ T_e &= \frac{T_{t,e}}{1 + \left[\frac{\gamma-1}{2}\right] M_e^2} \\ h_e &= C_p T_e \\ u_e &= \sqrt{2\left(h_{t,e} - \mathrm{h_e}\right)} \\ \rho_e &= \frac{P_e}{R T_e}, \end{aligned} \tag{38}$$

where u_e is the stream velocity at the exit, R is the ideal gas constant.
Area ratio:

$$\frac{A_0}{A_n} = \frac{M_\infty \left[\frac{\gamma+1}{2\left(1+\frac{\gamma-1}{2}M_\infty^2\right)} \right]}{M_e \left[\frac{\gamma+1}{2\left(1+\frac{\gamma-1}{2}M_e^2\right)} \right]} \frac{P_{t,e}}{P_{t0}} \sqrt{\frac{T_{t,e}}{T_{t0}}}, \tag{39}$$

where $\frac{A_0}{A_e}$ is the area ratio between is inlet and outlet.

8. Thrust

This section used the Cantwell method [19] to calculate the thrust of turbofan engine.
Thrust flow constant:

$$\begin{aligned} C_{\text{core}} &= \frac{1}{1+\beta} \\ C_{\text{fan}} &= \frac{\beta}{1+\beta} \end{aligned} \tag{40}$$

Engine nondimensional thrust (*Cantwell* method):

$$\begin{aligned} F_{\text{nd,core}} &= C_{\text{core}} \left[\gamma \left[\frac{u_{e,\text{core}}}{v_\infty} - 1 \right] M_\infty^2 + \frac{A_{\infty,\text{core}}}{A_{\text{n,core}}} \left[\frac{P_e}{P_0} - 1 \right] \right] \\ F_{\text{nd,fan}} &= C_{\text{fan}} \left[\gamma \left[\frac{u_{e,\text{fan}}}{v_\infty} - 1 \right] M_\infty^2 + \frac{A_{\infty,\text{fan}}}{A_{\text{n,fan}}} \left[\frac{P_e}{P_0} - 1 \right] \right] \\ F_{\text{nd,turbofan}} &= F_{\text{nd,core}} + F_{\text{nd,fan}} \end{aligned} \tag{41}$$

Specific thrust & specific impulse:

$$\begin{aligned} F_{\text{sp}} &= \left(\frac{1}{\gamma M_\infty} \right) F_{\text{nd,turbofan}} \\ I_{\text{sp}} &= F_{\text{sp}} \cdot a_\infty \frac{1+\beta}{fg} \end{aligned} \tag{42}$$

Thrust specific fuel consumption:

$$\begin{aligned} \text{TSFC} &= \frac{1}{I_{\text{sp}}} \left(1 - \text{SFC}_{\text{adj}}\right) \cdot hr \\ \text{TSFC} &= \frac{fg(1 - \text{SFC}_{\text{adj}})}{(F_{\text{sp}} a_\infty (1+\beta))} \cdot hr \end{aligned} \tag{43}$$

Mass flow rate:
(Core flow sizing)

$$\begin{aligned} \dot{m}_{\text{core,size}} &= \frac{F_{\text{design}}}{F_{\text{sp}} a_\infty \left(1+\beta\right) \eta_{\text{throttle}}} \\ \dot{m}_{\text{nd}} &= \frac{\dot{m}_{\text{core,size}}}{\sqrt{\frac{T_{\text{ref}}}{T_{t5,\text{ground}}}} \left[\frac{P_{t5,\text{ground}}}{P_{\text{ref}}} \right]} \end{aligned} \tag{44}$$

(Core mass flow)

$$\dot{m}_{\text{core}} = \frac{\dot{m}_{\text{nd}}}{\sqrt{\frac{T_{\text{ref}}}{T_{t5}}} \left[\frac{P_{t5}}{P_{\text{ref}}} \right]} \tag{45}$$

where η_{throttle} is the throttle setting at each control point, $T_{\text{ref}} = 288.15$ K and $P_{\text{ref}} = 101.325$ kPa is the international standard natural gas reference temperature and pressure.
Thrust (2-Dimensional):

$$F_{\text{turbofan}} = F_{\text{sp}} \cdot a_\infty \cdot \dot{m}_{\text{core}} \cdot (1+\beta) \cdot \eta_{\text{throttle,turbofan}} \cdot \#\,\text{Eng} \tag{46}$$

Fuel flow rate:

$$\dot{m}_f = F_{\text{turbofan}} \frac{\text{TSFC}}{g} \tag{47}$$

Engine power:

$$\text{Power} = F_{\text{turbofan}} \cdot v_\infty \tag{48}$$

Acknowledgments

Authors are grateful to Professor Li Qiao from Purdue University, School of Aeronautics and Astronautics, for the discussion and advice about engine models.

References

[1] Lukaczyk, T. W., Wendorff, A. D., Colonno, M., Economon, T. D., Alonso, J. J., Orra, T. H., and Ilario, C., "SUAVE: an open-source environment for multi-fidelity conceptual vehicle design," *16th AIAA/ISSMO Multidisciplinary Analysis and Optimization Conference*, 2015, p. 3087.

[2] Sarlioglu, B., and Morris, C. T., "More electric aircraft: Review, challenges, and opportunities for commercial transport aircraft," *IEEE transactions on Transportation Electrification*, Vol. 1, No. 1, 2015, pp. 54–64.

[3] Bozhko, S., Hill, C. I., and Yang, T., "More-electric aircraft: Systems and modeling," *Wiley encyclopedia of electrical and electronics engineering*, 2018, pp. 1–31.

[4] Hall, D. K., Huang, A. C., Uranga, A., Greitzer, E. M., Drela, M., and Sato, S., "Boundary layer ingestion propulsion benefit for transport aircraft," *Journal of Propulsion and Power*, Vol. 33, No. 5, 2017, pp. 1118–1129.

[5] Kratz, J. L., and Thomas, G. L., "Dynamic analysis of the STARC-ABL propulsion system," *AIAA Propulsion and Energy 2019 Forum*, 2019, p. 4182.

[6] Gohardani, A. S., Doulgeris, G., and Singh, R., "Challenges of future aircraft propulsion: A review of distributed propulsion technology and its potential application for the all electric commercial aircraft," *Progress in Aerospace Sciences*, Vol. 47, No. 5, 2011, pp. 369–391.

[7] Benzaquen, J., He, J., and Mirafzal, B., "Toward more electric powertrains in aircraft: Technical challenges and advancements," *CES Transactions on Electrical Machines and Systems*, Vol. 5, No. 3, 2021, pp. 177–193.

[8] Pargett, D. M., and Ardema, M. D., "Flight path optimization at constant altitude," *Journal of guidance, control, and dynamics*, Vol. 30, No. 4, 2007, pp. 1197–1201.

[9] Park, S. G., and Clarke, J.-P., "Vertical trajectory optimization to minimize environmental impact in the presence of wind," *Journal of Aircraft*, Vol. 53, No. 3, 2016, pp. 725–737.

[10] Bonami, P., Olivares, A., Soler, M., and Staffetti, E., "Multiphase mixed-integer optimal control approach to aircraft trajectory optimization," *Journal of Guidance, Control, and Dynamics*, Vol. 36, No. 5, 2013, pp. 1267–1277.

[11] Lindner, M., Rosenow, J., and Fricke, H., "Aircraft trajectory optimization with dynamic input variables," *CEAS Aeronautical Journal*, Vol. 11, No. 2, 2020, pp. 321–331.

[12] Altus, S., and Kroo, I., "Concurrent wing design and flight-path optimization using optimizer-based decomposition," *7th AIAA/USAF/NASA/ISSMO Symposium on Multidisciplinary Analysis and Optimization*, 1998, p. 4920.

[13] Falck, R. D., Chin, J., Schnulo, S. L., Burt, J. M., and Gray, J. S., "Trajectory optimization of electric aircraft subject to subsystem thermal constraints," *18th AIAA/ISSMO Multidisciplinary Analysis and Optimization Conference*, 2017, p. 4002.

[14] "Boeing Airplane Characteristics for Airport Planning," , Mar 2023. URL `https://www.boeing.com/commercial/airports/plan_manuals.page`.

[15] Welstead, J., and Felder, J. L., "Conceptual design of a single-aisle turboelectric commercial transport with fuselage boundary layer ingestion," *54th AIAA aerospace sciences meeting*, 2016, p. 1027.

[16] Menner, M., Chakrabarty, A., Berntorp, K., and Di Cairano, S., "Learning Optimization-based Control Policies Directly from Digital Twin Simulations," *2022 IEEE Conference on Control Technology and Applications (CCTA)*, 2022, pp. 895–900.

[17] Bayen, A. M., Mitchell, I. M., Oishi, M. M., and Tomlin, C. J., "Aircraft autolander safety analysis through optimal control-based reach set computation," *Journal of Guidance, Control, and Dynamics*, Vol. 30, No. 1, 2007, pp. 68–77.

[18] McDonald, R. A., and Gloudemans, J. R., "Open Vehicle Sketch Pad: An Open Source Parametric Geometry and Analysis Tool for Conceptual Aircraft Design," *AIAA SCITECH 2022 Forum*, 2022, p. 0004.

[19] Cantwell, B. J., "Aircraft and rocket propulsion," *AA283 course*, 2010.

[20] Hill, P. G., and Peterson, C. R., "Mechanics and thermodynamics of propulsion," *Reading*, 1992.

[21] "CFM56 - CFM international jet engines," , Oct 2022. URL https://www.cfmaeroengines.com/engines/cfm56/.

[22] "14 CFR 91.117 Aircraft Speed," , Aug 1989. URL https://www.ecfr.gov/current/title-14/chapter-I/subchapter-F/part-91/subpart-B/subject-group-ECFRe4c59b5f5506932/section-91.117.

[23] "Boeing Airplane Characteristics for Airport Planning," , Dec 2010. URL https://www.boeing.com/commercial/airports/plan_manuals.page.

[24] Wakefield, I., and Dubuque, C., "Exceeding Tire Speed Rating During Takeoff," , 2009. URL https://www.boeing.com/commercial/aeromagazine/articles/qtr_02_09/pdfs/AERO_Q209_article04.pdf.

[25] Cantwell, B. J., "AA283Aircraft and Rocket Propulsion Course Book," , Jul 2022. URL https://web.stanford.edu/~cantwell/AA283_Course_Material/AA283_Lectures/AA283_Course_Introduction_Brian_J_Cantwell.pdf.